Performance Characteristics of Scaled Bilayer Graphene Pseudospin Devices

M. J. Gilbert, *Member, IEEE*

Abstract—In this paper, we examine the performance characteristics of bilayer graphene pseudospin devices as we scale the layer width of the monolayers of graphene which comprise the bilayer structure. We find that, for layer widths of 30 nm, the device performance can exceed analytical predictions due to thermal smoothing of the interlayer interactions. However, when the device is further scaled to 20 nm and below, we find an appreciable drop of the maximum current the device can sustain when compared with the predicted values which result from increased quantum interference between injected quasi-particles and those reflected off of the excitonic gap opened at the Fermi energy. These results provide important insight into the maximum achievable performance characteristics and optimal device-design parameters for this promising potential post-CMOS logic device.

Index Terms—Beyond complementary metal–oxide–semiconductor (CMOS), bilayer, graphene, nanoelectronics, tunneling.

I. INTRODUCTION

THE SILICON metal–oxide–semiconductor (MOS) field-effect transistor (MOSFET) has been a staple of the semiconductor industry for more than 30 years. In response to the need for ever smaller devices, the MOSFET has undergone many generations of scaling to improve the performance and extend the life of complementary MOS (CMOS) technology. Nevertheless, efforts to increase the MOSFET's performance can no longer be achieved by simply making the salient feature sizes in the device smaller. To extend the life of CMOS, significant efforts have been explored to augment the traditional silicon planar technology through the addition of multiple gates for better electrostatic control over the device. The penultimate example of this effort is realized when the addition of multiple gates is coupled with advances in fabricating nanowires to produce a trigate nanowire transistor [1], [2]. While this does reduce the tunneling currents that plague the planar MOSFETs, the energy required to switch the device is greater than the planar version [3]. This is a result of the fact that the carrier mobility is decreased due to the confinement of enhanced phonon scattering present in these structures, and it offsets the gains made in the device electrostatics. Additionally, current silicon-technology designs also utilize modifications made to the device channel. These modifications are through strain [4] or using different high-κ gate stacks [5]. The effect of strain on the system is to alter the silicon bandstructure to decrease the effective mass of the carriers, thereby increasing the mobility and overall device performance. Meanwhile, the use of high-κ gate stacks allows better electric-field penetration from the gate when compared with that of SiO_2 which allows for the use of thicker oxides, effectively increasing control over the channel by reducing the parasitic gate current. While both of these modifications are successful in their objectives, they lead to only modest gains in device performance and modest reductions in the overall power consumption as they both suffer from increased scattering from defects and dislocations, which offset the majority of the gains.

Not only are new designs being explored in silicon to extend the life of CMOS but also, new materials are being explored to replace silicon as the channel material. One approach is to use III–V semiconductors, such as InAs [6] or InSb [7], due to their high mobilities compared with that of silicon. Furthermore, these materials are predicted to behave ballistically over larger length scales at room temperature than that of silicon. Therefore, using these materials as channel replacement materials has the potential to show large improvements in device speed and output current. However, implementations have met with limited success due to the low density of states of the III–V systems compared with similar silicon technologies [8], [9].

Yet, each of these approaches to extend the life of CMOS suffer from a common problem in that they all operate based on the same device physics. Even if any of these previous approaches were to work ideally, the subthreshold slope can only be 60 mV/dec. Clearly, in the search for a low-power CMOS logic alternative, there has been a significant effort to seek solutions in materials and systems beyond those traditionally explored systems presented earlier. These include the following: molecular [10], single-electron transistors [11], and carbon nanotubes (CNTs) [12], [13]. Of these different systems, the most popular and most successful has been CNTs. CNTs have demonstrated nearly ideal switching characteristics, increased device speed, and lower power consumption than that of traditional planar silicon logic by utilizing band–band tunneling; however, their implementation has been significantly impeded by the fact that there still exists no solution to sort the metallic CNTs from the semiconducting ones. Until this problem is resolved, CNTs will not be useful logic devices.

A particularly attractive way to solve the power-consumption problem in next-generation logic devices is by harnessing the collective motion of electrons. Current MOSFET technology is based on a set of independently moving electrons. Switching

This article has been accepted for inclusion in a future issue of this journal. Content is final as presented, with the exception of pagination.

2   IEEE TRANSACTIONS ON ELECTRON DEVICES

requires a change in gate voltage large enough to shift each electron's energy by more than the room-temperature thermal energy. With collective motion of electrons, one may hope to achieve switching with smaller changes in gate voltage: The energy of an entire ensemble of electrons can be shifted by more than the room-temperature thermal energy, turning on transport, even though each electron's energy is shifted by only a small fraction of that amount. One of the most spectacular demonstrations of collective behavior in the last ten years is the giant enhancement in tunnel current in semiconductor bilayer devices in the quantum Hall regime [14]. The enhanced tunnel current between the two layers occurs when electrons in the top layer bind with vacancies in the bottom layer to form "indirect excitons," which in turn organize into a Bose–Einstein condensate (BEC). This type of behavior may be viewed as spontaneous coherence: selection of a particular superposition of states in the two layers for the entire system. While this type of behavior is normally found only at very low temperatures and in large magnetic fields, recent work has shown that it is possible to find spontaneous coherence at and above room temperature in bilayer graphene devices when one layer contains only electrons, and the other layer contains an equal number of holes [15]–[17].

We believe that the existence of such an effect would make a very effective post-CMOS switch. We envision that the switch would operate in by setting the bottom layer gate voltage to contain a large number of holes with the top layer gate voltage initially unbiased. We apply a small interlayer bias so as to drive an interlayer current from the top layer to the bottom layer. At this point, the device would be in the "OFF" state as there would be only a few stray carriers in the top layer, and the only interlayer current observable would be some small single-particle tunneling events. As we begin to increase the voltage on the top layer, populating the top layer with more electrons, the interlayer exchange begins to enhance the tunneling current. This process continues until we reach the "ON" state of our device when the layer quasi-particle densities are balanced, and the strongly correlated state forms produce a maximal interlayer current. This process would create a transfer characteristic that is very reminiscent of an I_D–V_G trace in a traditional MOS transistor. While we would envision a subthreshold slope that is much less than the theoretical limit of 60 mV/dec seen in MOSFETs, we do not, at present, understand how quickly the interlayer-exchange enhancement amplifies the interlayer tunneling current. It is this property which will set the switching energy of our device. Therefore, switching from off to on would be accomplished by switching the top gate voltage from no bias to the equal and opposite bias of the bottom layer voltage.

Recent work has examined different possible logic devices which could be realized if such a device were to be fabricated experimentally using an assumed set of transfer characteristics [18], [19]. In this paper, we seek to expand the understanding of how such a device would perform at room temperature under an otherwise ideal set of conditions by examining the interlayer-transport characteristics through the use of quantum transport simulations based on the popular nonequilibrium Green's function technique. In particular, we study the effect of scaling the layer width in the interlayer currents. We find
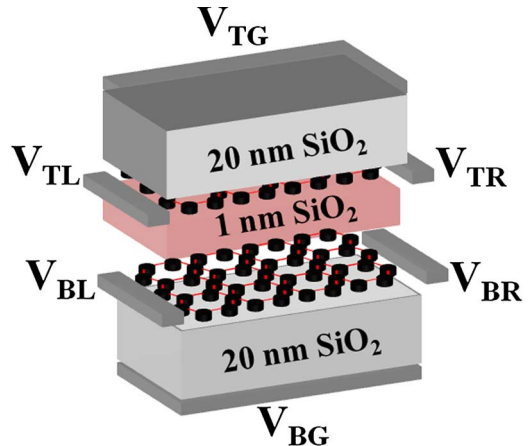

Fig. 1. Schematic of the bilayer graphene device under consideration in this paper. We have two monolayers of graphene separated by 1 nm of SiO_2. The device has top and bottom gates which are separated from the graphene by an additional 20 nm of SiO_2. We place contacts on the left and right edges of the top (V_{TL}, V_{TR}) and bottom (V_{BL}, V_{BR}) graphene layers through which we may inject and extract current.

that, for layer widths in excess of 20 nm, the device behaves in much the same way as has been previously predicted in that the device can sustain larger interlayer currents than previously predicted due to thermal smoothing of the interlayer interactions. However, when the layers reach a width of 20 nm, we find that the maximum device current drops by almost one order of magnitude due to the presence of strong quantum-interference effects which serve to energetically separate the two layers. These results provide important insight into the maximum achievable performance characteristics and optimal device-design parameters for this potential post-CMOS logic device.

II. DEVICE STRUCTURE AND SIMULATION METHOD

In Fig. 1, we show a schematic of the bilayer graphene device that we consider in this paper. Here, we have two monolayers of graphene separated from one another by a thin tunnel dielectric consisting of 1 nm of SiO_2. We have top and bottom gates V_{TG} and V_{BG}, respectively, which are isolated from the graphene layers by 20 nm of SiO_2. We utilize the top and bottom gates to draw carriers into the graphene layers. We connect the left and right edges of the top and bottom layers with contacts through which we may inject and extract current. The length of the graphene monolayers is set to 100 nm for the remainder of this paper, and we set the system temperature to room temperature, or $T_{system} = 300$ K. The width of the graphene layers will be varied throughout the remainder of this paper from 10 to 40 nm. We set the top and bottom gate voltages to be $V_{TG} = -V_{BG} = 0.4$ V, which correspond to an electron and hole concentration of 1×10^{13} cm^{-2}, which is the maximum quasi-particle density that the graphene layers may maintain before breakdown [20]. To maximize the flow of the superfluid in our system, we choose the drag–counterflow bias configuration [21]. In this bias configuration, the contacts are biased with $V_{TL} = V_{IL}$ and $V_{TR} = -V_{IL}$, while $V_{BL} = V_{BR} = 0$ V. In this way, we will drive electrons from the top layer to the bottom layer on the left side of the device, while at the same time, we drive holes

This article has been accepted for inclusion in a future issue of this journal. Content is final as presented, with the exception of pagination.

GILBERT: PERFORMANCE CHARACTERISTICS OF BILAYER GRAPHENE PSEUDOSPIN DEVICES 3

from the top layer to the bottom layer. The currents that we plot are the currents which travel from V_{TL} to V_{BL}, where V_{IL} is the interlayer voltage. Additionally, before we descend into the specifics of simulating such as system, we must define our axes. Here, we take $\hat{x}$ to be along the length of the device, $\hat{y}$ to be along the width of the device, and $\hat{z}$ to be in the depth direction. We assume that the top and bottom layers are perfectly registered with one another, and the transport is ballistic in nature.

With the device structure set, we now outline the system Hamiltonian that we use to elucidate the salient performance characteristics of this device. We begin by defining the Hamiltonian for each layer [22], [23]

$$H_{\text{layer}} = \sum_{i,j} \tau_{i,j} |i\rangle\langle j| + V|i\rangle\langle i| \tag{1}$$

where, in (1), $\tau_{i,j} = -\tau = -3.03$ eV if the orbitals corresponding to locations $|i\rangle$ and $|j\rangle$ are nearest neighbors on the honeycomb lattice, of which each atom has three nearest neighbors in graphene, otherwise $\tau_{i,j} = 0$ eV. The resulting bandstructure from the layer Hamiltonian is the well-known linear bandstructure for low-energy excitations with two minima at the K and K' points in the Brillouin zone. Due to this unique bandstructure, the quasi-particle excitations are equivalent to Dirac quasi-particles or, equivalently, Weyl neutrinos [22]. The $V|i\rangle\langle i|$ term in (1) represents the Hartree term for each position in the layer. In this paper, we assume that the top layer and the bottom layer are perfectly registered with one another. This assumption is a reasonable one due to the fact that the two layers are not in physical contact with one another. From the simple definition of the layer Hamiltonian, we can extend this to the definition of the system Hamiltonian as

$$H_{\text{system}} = \begin{bmatrix} H_{\text{TL}} & \vec{\Delta} \\ \vec{\Delta} & H_{\text{BL}} \end{bmatrix}. \tag{2}$$

Here, the diagonal portions of (2) represent the layer Hamiltonians for the top and bottom layers H_{TL} and H_{BL}, respectively, and the off-diagonal terms $\vec{\Delta}$ represent the interlayer interactions. In order to represent the interlayer interactions, we utilize pseudospin notation where the "which-layer" degree of freedom is mapped into a spin-1/2 quasi-particle with pseudospin up $|\uparrow\rangle$ representing the top layer and pseudospin down $|\downarrow\rangle$ representing the bottom layer. The interlayer interactions we describe here are composed of both single-particle interactions and many-body interactions. The single-particle interlayer tunneling term Δ_{sas} contributes an effective field to the system Hamiltonian in the $\hat{x}$ direction. This interaction contribution arises from the fact that interactions contribute a Zeeman field to the Hamiltonian of a spin-polarized gas which is oriented in the same direction as the spin polarization. The interaction contribution to the interlayer transport can be derived by expanding the energy functional obtained by minimizing the ground state Hartree–Fock trail wavefunction for the many-body system around the supercurrent state, as has been done previously in the case of semiconducting bilayers in the quantum Hall regime [24]. Graphene bilayers with pseudospin polarization due to tunneling have a similar contribution to the

Hamiltonian. We can write down the interaction contribution to the Hamiltonian, including both single particle and many-body contributions, as [25], [26]

$$\vec{\Delta} = \Delta_{\text{sas}}\hat{x} + U m_{\text{exc}} \left[\cos(\varphi_{\text{exc}}), \sin(\varphi_{\text{exc}})\right]. \tag{3}$$

In (3), $\vec{m}_{\text{exc}}$ is the magnitude of the pseudospin polarization and is defined as

$$\vec{m}_{\text{exc}} = \frac{1}{2\nu_0} Tr[\rho\tau] \tag{4}$$

where, in (4), ρ is the Hermitian 2×2 pseudospin density matrix

$$\rho = \begin{bmatrix} \rho_{\uparrow\uparrow} & \rho_{\uparrow\downarrow} \\ \rho_{\downarrow\uparrow} & \rho_{\downarrow\downarrow} \end{bmatrix} \tag{5}$$

and $\tau = (\sigma_x, \sigma_y, \sigma_z)$ is the vector of Pauli spin matrices and ν_0 is the layer density of states. In (3), φ_{exc} is the planar orientation of the pseudospin magnetism on the pseudospin Bloch sphere, and U is the on-site Coulomb interaction. As a result of the multiplications performed in (4), $\vec{m}_{\text{exc}}$ has three directional components: m_{exc}^x, m_{exc}^y, and m_{exc}^z. The $\hat{x}$ and $\hat{y}$ directional pseudospin fields may be obtained by examining the pseudospin density matrix as

$$m_{\text{exc}}^x = \rho_{\uparrow\downarrow} + \rho_{\downarrow\uparrow}$$
$$m_{\text{exc}}^y = -i\rho_{\uparrow\downarrow} + i\rho_{\downarrow\uparrow}. \tag{6}$$

From the directional pseudospin fields obtained in (6), we may combine these expressions to obtain the planar orientation of the pseudospin magnetism φ_{exc} by

$$\varphi_{\text{exc}} = \tan^{-1}\left(\frac{m_{\text{exc}}^y}{m_{\text{exc}}^x}\right). \tag{7}$$

However, we still need to identify the $\hat{z}$-directed component of the pseudospin field which is a measure of the screening between the top and bottom layer and serves to energetically separate the nested Fermi surfaces [23], [25], [26]. This component is simply the difference between the top and bottom layer self-consistent potentials or

$$m_{\text{exc}}^z = \frac{\rho_{\uparrow\uparrow} - \rho_{\downarrow\downarrow}}{2} = \frac{V_\uparrow|i\rangle\langle i| - V_\downarrow|i\rangle\langle i|}{2}. \tag{8}$$

We may collect all the interaction contributions and rewrite (3) in expanded notation as

$$\vec{\Delta} = (\Delta_{\text{sas}} + U m_{\text{exc}}^x) \sigma_x + U m_{\text{exc}}^y \sigma_y + m_{\text{exc}}^z \tag{9}$$

where σ_x, σ_y, and σ_z are the $\hat{x}$-, $\hat{y}$-, and $\hat{z}$-directed Pauli matrices. The only remaining part of the Hamiltonian left to be addressed is the on-site Coulomb term U in the interaction contribution. This term deals with the amount of exchange enhancement existing between the two layers when the layers have an equal number of electrons in the top layer as holes in the bottom layer. As this is a term which is inherently many body in nature, single-particle techniques, even those which propagate the Hamiltonians containing many-body terms, cannot accurately capture the strength of the exchange enhancement

This article has been accepted for inclusion in a future issue of this journal. Content is final as presented, with the exception of pagination.

4   IEEE TRANSACTIONS ON ELECTRON DEVICES

of the coupling between the two layers resulting from the strong interlayer Coulomb interactions. Therefore, we utilize the interlayer exchange enhancement as calculated by other mean-field methods [16], [17], and, for the remainder of this paper, we set the value of the on-site Coulomb interaction to be

$$U \approx 0.1 E_F. \tag{10}$$

Now, with the Hamiltonian completely specified, we calculate the transport properties of this system using standard self-consistent process. To find the single-particle density matrix of the 2-D system, we must evaluate the quasi-particle Hamiltonian where the interactions are modeled in the local density approximation we outlined earlier. We do so using a Greens'-function-based method in a real-space tight-binding basis, as done previously [22], [23], [26]. The electrostatic potential throughout the system is calculated from the charge density in each of the 2-D layers by solving the Poisson equation in three dimensions with the appropriate boundary conditions. The solution of the full 3-D Poisson equation is necessary to correctly account for the interlayer and intralayer interactions which arise in the Hartree term in (1) and (2). The boundary conditions that we employ in this paper are hard-wall boundary conditions on the top, bottom, and sides of the simulation domain and open boundary conditions at the contacts. The use of hard-wall boundary conditions here is justified by the fact that the edges of the graphene ribbons are armchair, and both the A sublattice and B sublattice wavefunctions go to zero at the edges in an armchair configuration. Once we obtain the single-particle density matrix, we update the density in the Poisson solution via the Broyden method [27] to help accelerate self-consistency between the transport and electrostatic equations. We iterate over the Poisson equation and the transport kernel until we have a difference in old and new potentials which is less than the single-particle splitting Δ_{sas} to ensure accurate results. Once self-consistency has been achieved, we compute the currents via the Landauer formula at finite temperature, i.e.,

$$I_{\mathrm{IL}}(V_{\mathrm{IL}}) = \frac{2e}{h} \int T(E) \left[f_\uparrow(E) - f_\downarrow(E) \right] dE. \tag{11}$$

III. WIDTH DEPENDENCE OF INTERLAYER TRANSPORT

Before we examine the interlayer-transport characteristic, it is important to define a few important quantities which will be very useful in analyzing the transport in our correlated system. In Fig. 2, we show a schematic of the charge injection (a) into a superconductor and (b) into our bilayer system. In Fig. 2(a), we show a superconductor system with two normal metallic contacts attached on the left- and right-hand sides of the system. Now, consider the physical processes at work when we apply a small bias across the system which causes a single charge to be injected from the left contact and propagate toward the right contact. In a superconductor, pairing between electrons occurs in a small energy range about the Fermi energy. As a result of the Cooper instability, an energy gap opens about the Fermi energy. The resulting charge that we inject from the left contact will be injected directly into this energy gap. The electron will penetrate into the superconductor over a
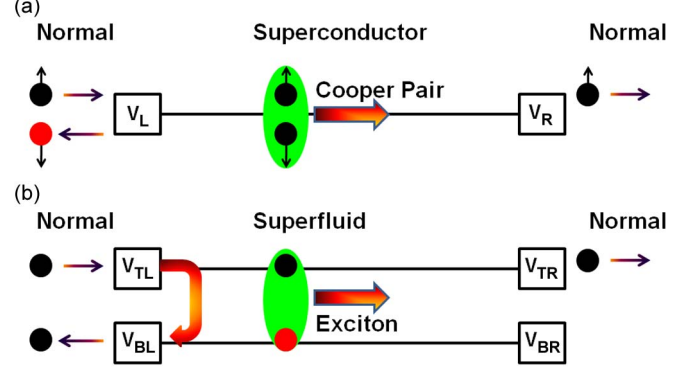

Fig. 2. (a) Schematic of normal metallic contact–superconductor–normal metallic contact geometry where we illustrate the process of (black) an incident electron from the left contact undergoing the process of an Andreev reflection. When the incident electron reaches the normal–superconductor interface, it is reflected back as (red) a hole with opposite spin, and a Cooper pair is launched in the superconductor to conserve total current. When the electron reaches the right contact, the supercurrent is converted back into an electron quasi-particle current. (b) Schematic of the bilayer device that we consider in this paper, where we illustrate (black) a single incident electron in the top left contact. As the electron enters the superfluid region in the bulk of the device, it undergoes a process similar to an Andreev reflection where it is reflected off of the superfluid region and returns as an electron in the bottom layer. To conserve the total current, an exciton is launched across the system. As the exciton reaches the right contact, it is converted back into an electron quasi-particle current.

characteristic distance, referred to as the Josephson length, and then it is reflected back to the left contact as a hole with opposite spin. To conserve the overall current across the superconducting system, a Cooper pair, composed of a spin-up and spin-down electron, is launched across the superconductor. This process is referred to as an Andreev reflection. As the Cooper pair reaches the right contact, it again undergoes a reflection, and the supercurrent is converted back into a quasi-particle which then flows out of the system. In Fig. 2(b), we have a situation that is very similar to the case in Fig. 2(a), with the normal-metal–superconductor–normal-metal system. In our bilayer, we have equal and opposite momentum in the two layers, and a gap in the allowed eigenstates will open up about the Fermi energy. Therefore, as the quasi-particles are injected into the system from the top left contact, they will reflect off of this gap in much the same way that quasi-particles are reflected off of the gap which opens in the energy spectrum of a superconductor due to the Cooper instability. Once reflected, a portion of the quasi-particles will be completely reflected back to the injecting contact, while the other portion of the particles will be transmitted to the bottom layer. To conserve current, the system will then launch an exciton which will propagate across the gapped section of the system until the exciton reaches the contacts at the opposite end of the structure. At this point, the exciton will recombine with the quasi-particles and exit the system via the contacts. The length that the quasi-particle may penetrate into the gapped region of the system is referred to as the coherence length L_C and is analogous to the Josephson length in a superconductor. In terms of the system parameters, we may define the coherence length as [17], [25]

$$L_C = \frac{1}{k_F} \sqrt{\frac{\langle m_{\mathrm{exc}}^x \rangle}{\Delta_{\mathrm{sas}}}}. \tag{12}$$

This article has been accepted for inclusion in a future issue of this journal. Content is final as presented, with the exception of pagination.

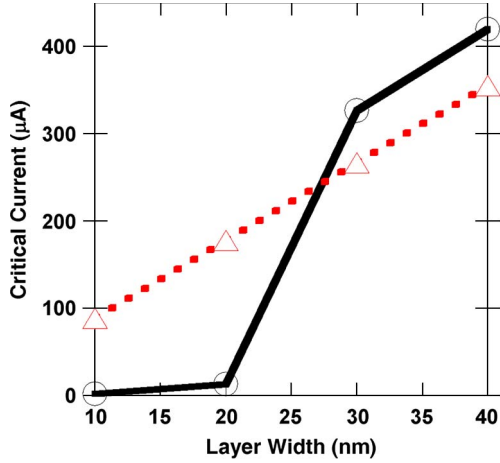GILBERT: PERFORMANCE CHARACTERISTICS OF BILAYER GRAPHENE PSEUDOSPIN DEVICES

5

Fig. 3. Plot of the critical currents calculated via (black) the numerical simulations and the critical currents calculated using (red) (13). We see that below a certain layer thickness, the critical current in the system drops below the analytic value.

Fig. 4. (a) Interlayer I–V characteristics and (b) interlayer differential conductance for layer widths of (black) 20 nm and (red) 30 nm corresponding to $V_{\mathrm{GT}} = -V_{\mathrm{GB}} = 0.4$ V calculated at room temperature. We see a very obvious discrepancy between the 20-nm layers and the 30-nm layers as evidenced by the smaller critical current.

In (12), k_F is the Fermi wave vector of the quasi-particles in graphene and $\langle m_{\mathrm{exc}}^x \rangle$ is the value of the longitudinally directed pseudospin field, also commonly referred to as the pseudospin stiffness. For our particular gate-voltage configuration of $V_{\mathrm{TG}} = -V_{\mathrm{BG}} = 0.4$ V, this results to $L_C = 10.47$ nm.

A second important quantity is the critical current. When the graphene system is in a BEC and we apply a bias, the system responds by adjusting the interlayer phase φ_{exc} to carry a current. The critical current refers to the maximum interlayer current which may be carried by the condensate. Utilizing previous definitions, we may describe the critical current [17], [20], [24] as

$$I_{\mathrm{crit}} = \frac{eA \langle m_{\mathrm{exc}}^x \rangle}{\hbar L_C^2} \qquad (13)$$

where A is the area of the graphene layer.

In Fig. 3, we show the main result of this section. Here, we show that the critical current in the bilayer graphene system has a width dependence which is not well coordinated with the analytical results in (13). While the simulations do not take into account important effects such as phonon scattering or graphene-edge roughness, we see that if this system is to be used as a post-CMOS logic device, care must be taken when designing them. Should the layer width be scaled too aggressively, there is an appreciable loss in device performance. For layer widths of 30 nm and above, we find that the system has a critical current which is 50% larger than the analytical value, as has been predicted previously [26]. This increase in critical current is due to thermal smoothing of the interlayer interactions, slowing the energy separation of the two nested Fermi surfaces. Yet, as we scale the layer width below 30 nm, we find that the critical current drops to values of only about 10% of the analytical value. One naively expects this to be a critical width where the Fermi surface becomes deformed from the expected 2-D Fermi surface due to the confinement; however, the Fermi wavelength in the system is still $\lambda_F = 1$ nm. Therefore, this should not be affecting our results. At widths of 30 nm, the magnitude of the critical current increase
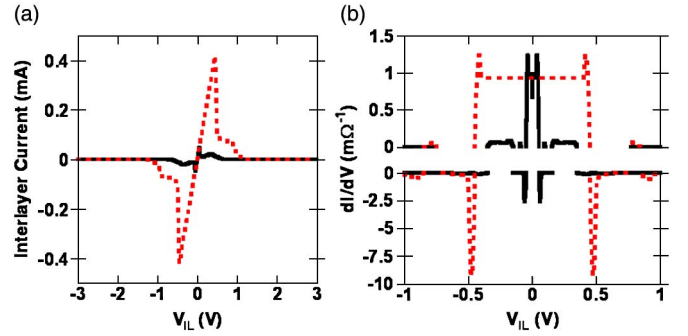
at elevated temperatures due to thermal smoothing of the interlayer interactions, so we would expect larger magnitudes for the critical currents in the 20-nm case, as well. As we are assuming that the quasi-particles here are moving ballistically, energy loss due to other phonon-related processes cannot be the culprit that is responsible for the reduction in the magnitude of the critical current.

We now examine the I–V characteristics in Fig. 4(a) corresponding to the 30-nm-wide sample (red) with a single-particle tunneling amplitude of $\Delta_{\mathrm{sas}} = 100~\mu$eV. We have chosen this value to be small enough so as to have a coherence length that is shorter than the length of our device and large enough so as not to require a great deal of self-consistent iterations in order to achieve energy resolutions below Δ_{sas}. Clearly, we see that the current varies linearly with the applied interlayer voltage before reaching the critical current. Here, we find that the magnitude of the critical current is $326.4 \pm 11.6~\mu$A compared with the 266.5 μA which is obtained using (13). The discrepancy between these two values is related to the thermal smoothing of the interlayer interactions at elevated temperatures [26]. Once the interlayer current exceeds the critical current, the interlayer conductivity of the system quickly drops, and the two layers behave as if they are noninteracting. In other words, the tunneling that we find in the system past the critical current is due to incoherent tunneling processes limited by Δ_{sas}.

This situation is to be contrasted with the curve representing the system with the 20-nm-wide graphene layers (black) in Fig. 4(a). In this situation, the magnitude of the calculated critical current is $12.9 \pm 8.1~\mu$A compared with the analytical value of $177.7~\mu$A. The variation of the current with the applied interlayer voltage is more clearly seen in Fig. 4(b) where we plot the differential interlayer conductance as a function of the applied interlayer bias. We may now clearly see the linear variation of the interlayer current with the interlayer voltage until we reach the critical current, and the interlayer conductivity drops quickly with increasing interlayer bias for both the 30-nm (red) and 20-nm (black) systems. We also notice the large discrepancy in the regime where the interlayer current may be supported by the BEC as we decrease the system width, with the differential interlayer conductance beginning to drop at $V_{\mathrm{IL}} = 0.07$ V compared with $V_{\mathrm{IL}} = 0.45$ V for the 30-nm case.

This article has been accepted for inclusion in a future issue of this journal. Content is final as presented, with the exception of pagination.

6   IEEE TRANSACTIONS ON ELECTRON DEVICES
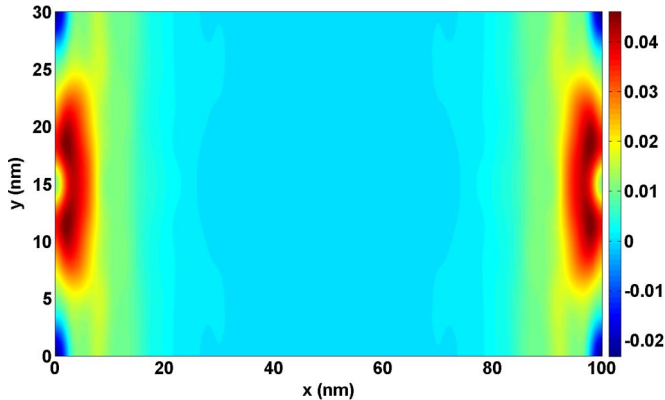

Fig. 5.   Plot of the longitudinal pseudospin field $\langle m_{\text{exc}}^x \rangle$ for $\Delta_{\text{sas}} = 100 \, \mu\text{eV}$ at an applied interlayer voltage of $V_{\text{IL}} = 0.07$ V as a function of position in the bilayer graphene system. The width of the layers in this system is 30 nm. We see that the value of the longitudinal pseudospin field is equivalent to that of the on-site Coulomb term U.

Fig. 6.   Plot of the transverse pseudospin field $\langle m_{\text{exc}}^y \rangle$ for $\Delta_{\text{sas}} = 100 \, \mu\text{eV}$ at an applied interlayer voltage of $V_{\text{IL}} = 0.07$ V as a function of position in the bilayer graphene system. The width of the layers in this system is 30 nm. We see that the value of the transverse pseudospin field are about an order of magnitude greater than that of the on-site Coulomb term U only near the point where the quasi-particles are injected into the system on the left-hand side.

To understand the reduction in the magnitude of the critical interlayer currents, we examine the directional pseudospin fields for the two separate situations. In Fig. 5, we show the value of the longitudinal pseudospin field $\langle m_{\text{exc}}^x \rangle$ for an interlayer voltage of $V_{\text{IL}} = 0.07$ V with $\Delta_{\text{sas}} = 100 \, \mu\text{eV}$. This value corresponds to the last bias voltage where we are able to obtain a self-consistent calculation, i.e., before the critical current in both the 20-nm and 30-nm cases. We see that the value of $\langle m_{\text{exc}}^x \rangle$ is very close to the value of the on-site Coulomb term U. We also note that the quasi-particles are allowed to penetrate further into the system than L_C before they are reflected or transmitted to the other layer. This is the result of the thermal broadening in the system allowing for many additional modes to be injected above the energy gap created by the formation of a condensate. The waves are injected and couple at either end of the system; however, their contribution is small compared with the many-body contribution to the interlayer current, and we see that the vast majority of the interlayer coupling observed in $\langle m_{\text{exc}}^x \rangle$ is within L_C after which the magnitude of $\langle m_{\text{exc}}^x \rangle$ decays rapidly to numbers which are on the order of magnitude smaller than that of Δ_{sas}. Furthermore, we also see the complicated form the pseudospin fields obtain as a function of position. This is a result of the interference of the injected states in the layers interfering with the states reflected off of the gap opened about the Fermi energy.

In Fig. 6, we plot the transverse pseudospin field $\langle m_{\text{exc}}^y \rangle$ as a function of position in the system for an interlayer voltage of $V_{\text{IL}} = 0.07$ V with $\Delta_{\text{sas}} = 100 \, \mu\text{eV}$. In this case, it seems that the transverse pseudospin field is equivalent to that of the longitudinal pseudospin field only within L_C of the left-hand side of the system where the electrons are injected. It appears to have no value at all after this point. However, this is counterintuitive, as the lack of an interlayer phase would imply that there is no current flowing in the system beyond L_C. A second striking feature is that the transverse pseudospin field is greater than the longitudinal pseudospin field by an order of magnitude near the injection site on the left-hand side of the system.

In Fig. 7, we show the interlayer phase, using (7), down the centerline of the system for $V_{\text{IL}} = 0.07$ V. We plot the interlayer phase simply down the centerline of the system
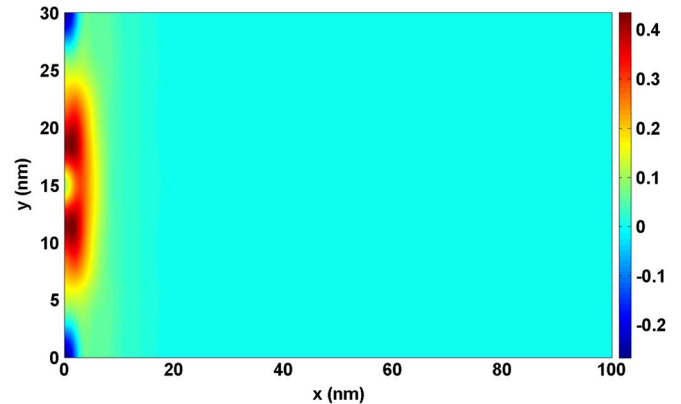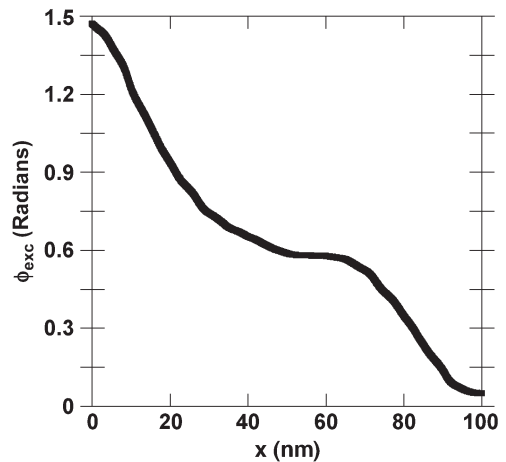

Fig. 7.   Plot of the interlayer phase φ_{exc}, plotted down the centerline of the system, as a function of the longitudinal position in our bilayer graphene system with layers that are 30 nm in width.

(at a width of 15 nm) rather than showing the full surface plot as the width direction of the layers does not have much variation when we calculate the interlayer phase. The variation, as we move across the width at any given length, is typically about 5% of the phase value shown in Fig. 7. We see that after penetrating a distance of L_C into the system, the interlayer phase does not vanish. Therefore, while the overall magnitude of the tunneling may tend to very small numbers, the phase does not. It is vital to observe this behavior as the gradient of this interlayer phase relationship is proportional to the velocity of the superfluid [28]. The near linear variation close to both ends of the sample denotes a superfluid propagating with a constant velocity. The velocity of the superfluid changes close to the center of the system. This is due to the fact that there is a competition between the many-body term in the Hamiltonian, which desires a linear phase gradient, and the single-particle tunneling term, which is trying to force a constant phase difference between the two layers. The end result is that the superfluid flows with a constant velocity close to the contacts but slows near the center of the system.
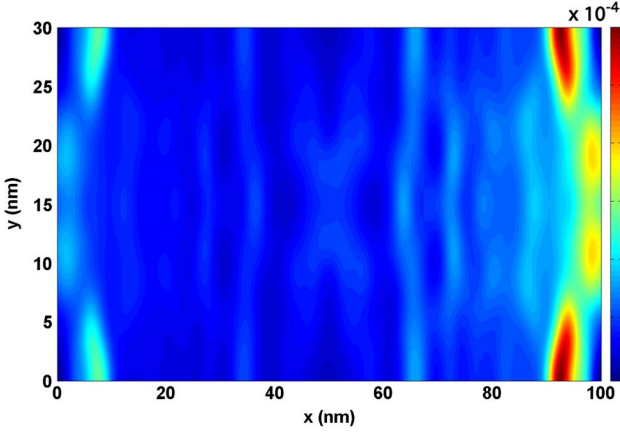
This article has been accepted for inclusion in a future issue of this journal. Content is final as presented, with the exception of pagination.

GILBERT: PERFORMANCE CHARACTERISTICS OF BILAYER GRAPHENE PSEUDOSPIN DEVICES 7

Fig. 8. Plot of the longitudinal pseudospin field $\langle m_{\mathrm{exc}}^x \rangle$ for $\Delta_{\mathrm{sas}} = 100 \ \mu$eV at an applied interlayer voltage of $V_{\mathrm{IL}} = 1.5$ V as a function of position in the bilayer graphene system. The width of the layers in this system is 30 nm. We see that the value of the longitudinal pseudospin field is now equivalent to that of the single-particle tunneling term Δ_{sas}.

Fig. 9. Plot of the transverse pseudospin field $\langle m_{\mathrm{exc}}^y \rangle$ for $\Delta_{\mathrm{sas}} = 100 \ \mu$eV at an applied interlayer voltage of $V_{\mathrm{IL}} = 1.5$ V as a function of position in the bilayer graphene system. The width of the layers in this system is 30 nm. We see that the value of the transverse pseudospin field is very small.

Fig. 10. Plot of the longitudinal pseudospin field $\langle m_{\mathrm{exc}}^x \rangle$ for $\Delta_{\mathrm{sas}} = 100 \ \mu$eV at an applied interlayer voltage of $V_{\mathrm{IL}} = 0.07$ V as a function of position in the bilayer graphene system. The width of the layers in this system is 20 nm. We see that the value of the longitudinal pseudospin field is equivalent to that of the on-site Coulomb term U at its maximum but that significant quantum-interference effects are now present.

With an understanding of the system behavior below the critical current, we now wish to examine the directional pseudospin fields when the system is beyond critical current. In Fig. 8, we plot the longitudinal pseudospin field $\langle m_{\mathrm{exc}}^x \rangle$ as a function of position. Now that the system is beyond critical current, we see some very stark differences between Figs. 5 and 8. The first difference between the two figures is in the magnitude of $\langle m_{\mathrm{exc}}^x \rangle$. In Fig. 5, we observed that the longitudinal pseudospin field self-consistently obtained a value which was close in value to the on-site Coulomb term. After the critical current, we know that the interlayer conductivity decreases rapidly. In Fig. 8, we find that the longitudinal pseudospin field has dropped more than two orders of magnitude and now obtains a value which is very close to the single-particle tunneling amplitude, Δ_{sas}. Therefore, after the critical current has been surpassed, the two layers look noninteracting with the current flow between the two layers being governed by single-particle incoherent tunneling events. A second observation concerning the longitudinal pseudospin field is that there is a slight asymmetry about the plot. This asymmetry denotes that the interlayer current at the ends of the sample is no longer identical. The lack of identical currents at the ends of the system shows that the gap in the excitation spectrum has closed and that some modes may propagate from the end of one layer to the other end of the same layer and tunnel from top to bottom, as is the case in normal single-particle physics and seen in other coupled systems [21]. This is corroborated by the fact that now, quasiparticle tunneling is not confined within L_C of the injection sites, and $\langle m_{\mathrm{exc}}^x \rangle$ now has appreciable magnitude over all of the system.

With such large changes in the longitudinal pseudospin field, we would expect to see equally interesting changes in the transverse pseudospin field. Indeed, in Fig. 9, we find that, over the entire system, the transverse pseudospin field has taken a very small value. This small value denotes a system which has no gradient in the overall interlayer phase resulting in no condensate flow from the left-hand side of the system to the right. This confirms that we are now in a regime dominated by single-particle tunneling and not correlated many-body effects.
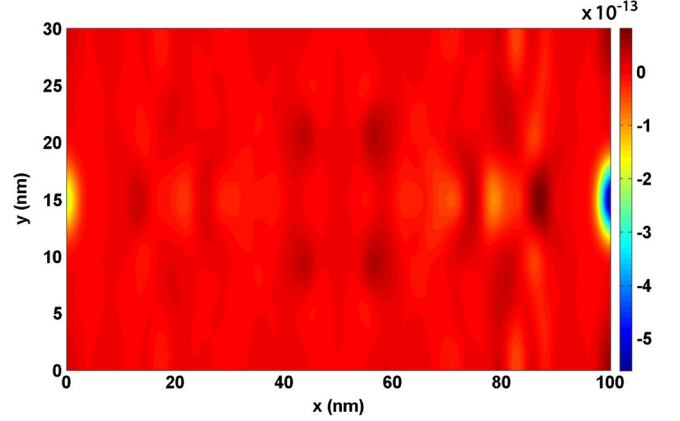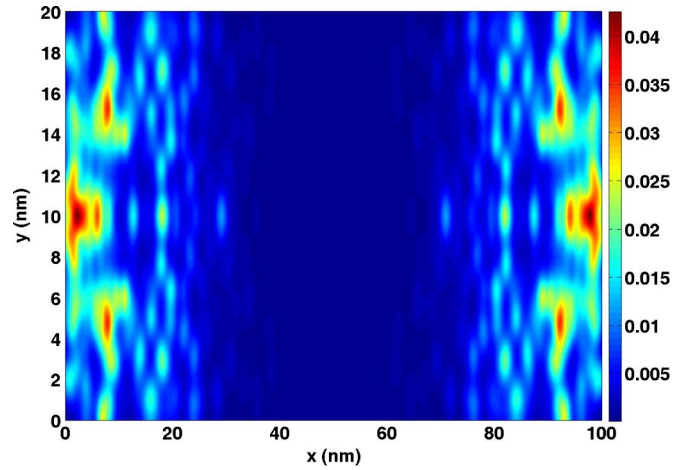
With an understanding of the general behavior of the 30-nm system, we can examine the longitudinal pseudospin fields of the 20-nm device to search for the root of the discrepancy in the interlayer transfer characteristics. To this end, we examine the longitudinal pseudospin field in the 20-nm system with $\Delta_{\mathrm{sas}} = 100 \ \mu$eV and an interlayer bias of $V_{\mathrm{IL}} = 0.07$ V as a function of position in Fig. 10. The first feature of this plot that appears different from the pseudospin field that we plot in Fig. 4 is that there are many more interference peaks in the structure. These peaks result from the reflection off of the gap about the Fermi energy which results from the interaction between the two layers. Instead of seeing one "hot spot" on either side of the system corresponding to the flow of quasiparticles between the two layers, the current flow between the two layers is now spread out in space. Furthermore, we also see that the interference produces sizable perturbations in the longitudinal pseudospin field. The interference peaks produce variations in the pseudospin field on the order of 50% of the value of the on-site Coulomb term. We also see that the
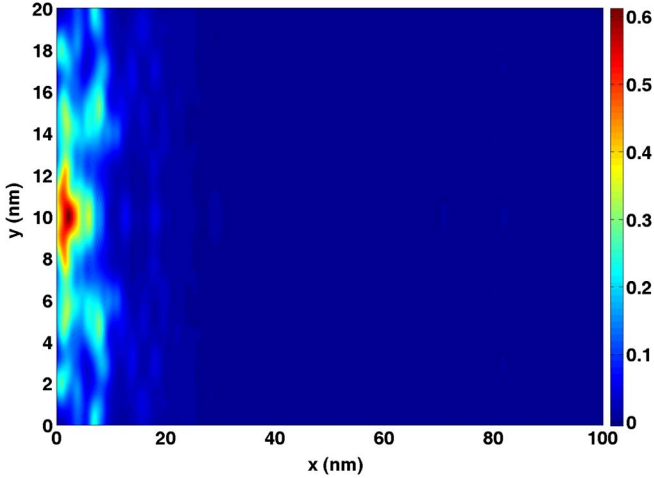
Fig. 11. Plot of the transverse pseudospin field $\langle m_{\mathrm{exc}}^{y} \rangle$ for $\Delta_{\mathrm{sas}} = 100$ μeV at an applied interlayer voltage of $V_{\mathrm{IL}} = 0.07$ V as a function of position in the bilayer graphene system. The width of the layers in this system is 20 nm. We see some of the effects of quantum interference here in the spatial variation of $\langle m_{\mathrm{exc}}^{y} \rangle$, but the overall phase is well behaved.

Fig. 12. Plot of the out-of-plane pseudospin field $\langle m_{\mathrm{exc}}^{z} \rangle$ for $\Delta_{\mathrm{sas}} = 100$ μeV at an applied interlayer voltage of $V_{\mathrm{IL}} = 0.07$ V as a function of position in the bilayer graphene system. The width of the layers in this system is 30 nm. We see only longitudinal variation in $\langle m_{\mathrm{exc}}^{z} \rangle$, and it only has a nonzero value over the first L_C away from the contacts.

Fig. 13. Plot of the out-of-plane pseudospin field $\langle m_{\mathrm{exc}}^{z} \rangle$ for $\Delta_{\mathrm{sas}} = 100$ μeV at an applied interlayer voltage of $V_{\mathrm{IL}} = 0.07$ V as a function of position in the bilayer graphene system. The width of the layers in this system is 20 nm. Quantum-interference effects produce large variations in $\langle m_{\mathrm{exc}}^{z} \rangle$ which work to separate the Fermi surfaces in energy.

quasi-particles which are injected into the system above the gap now have a more significant interlayer coupling in the center of the system, beyond a distance of L_C from either side. The value of $\langle m_{\mathrm{exc}}^{x} \rangle$ at its maximum is still on the same order of magnitude as the on-site Coulomb term, which is consistent with Fig. 4, and that we are still below the critical current, but the interference effects on $\langle m_{\mathrm{exc}}^{x} \rangle$ are undeniable.

Beyond the understanding of $\langle m_{\mathrm{exc}}^{x} \rangle$, we may also examine the behavior of the transverse pseudospin field. In Fig. 11, we plot $\langle m_{\mathrm{exc}}^{y} \rangle$ for $\Delta_{\mathrm{sas}} = 100$ μeV and an interlayer voltage of $V_{\mathrm{IL}} = 0.07$ V in a system with layer widths of 20 nm. As was shown in Fig. 6, we see that $\langle m_{\mathrm{exc}}^{y} \rangle$ is more than an order of magnitude greater than $\langle m_{\mathrm{exc}}^{x} \rangle$ near the left-hand side of the system close to the contacts, resulting in $\varphi_{\mathrm{exc}} \approx \pi/2$. Further, we also notice that this peak extends longitudinally roughly to a distance of L_C. We find that when we determine the overall phase of the system, it is very close in magnitude and gradient to that shown in Fig. 7. This is to be expected as the system response from both the 30-nm and 20-nm layer width systems results in the same interlayer current. We can see the signatures of the quantum interference seen in Fig. 10 in the spatial variation of the transverse pseudospin field; however, the self-consistent process results in an overall phase which is well behaved, as seen in Fig. 7. Therefore, the examination of the pseudospin fields yields no insight into why the smaller of the systems should reach the critical current so much sooner than the wider system.

To resolve this question, we do not look into the in-plane pseudospin fields but to the $\hat{z}$-directed component of the pseudospin fields $\langle m_{\mathrm{exc}}^{z} \rangle$ represented by (8). In Fig. 12, we plot the self-consistent potential for 30-nm layers with an interlayer voltage of $V_{\mathrm{IL}} = 0.07$ V. In both the 30-nm and the 20-nm layers, the system is still in an ordered pseudospin state. As the quasi-particles enter the system, the interactions resulting from the pseudospin torque effect [26] work to shift the pseudospin orientation from pseudospin up $|\uparrow\rangle$ to pseudospin down $|\downarrow\rangle$ along the left-hand side of the system or from pseudospin down
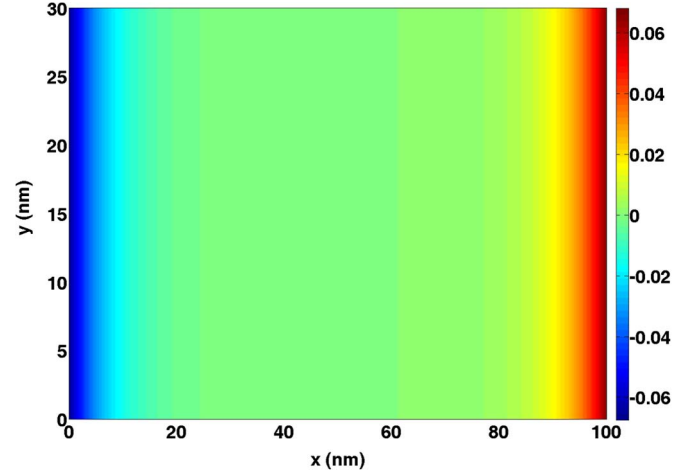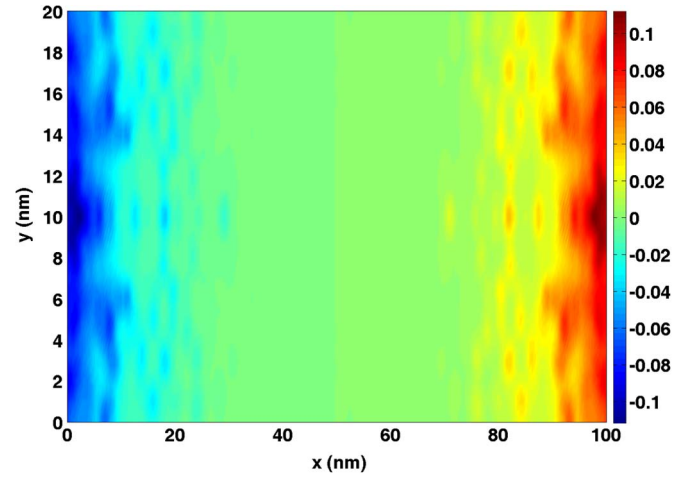
to up on the right-hand side of the system. We see very clearly in Fig. 12 that the pseudospin-torque term only acts on the quasi-particles over a distance of L_C away from the contacts. Beyond this distance, $\langle m_{\mathrm{exc}}^{z} \rangle$ decays to zero, at which point the quasi-particle flow is converted into supercurrent which flows in the bulk.

In Fig. 13, we contrast this simple picture of $\langle m_{\mathrm{exc}}^{z} \rangle$ in the 30-nm layers with $\langle m_{\mathrm{exc}}^{z} \rangle$ in the 20-nm layers. Here, we can see the effects of the quantum interference on the system very clearly. The quantum interference arising from reflections off of the gap in the bulk of the system disturbs $\langle m_{\mathrm{exc}}^{z} \rangle$ and results in a heavily spatially dependent field. We notice that the field now can be both larger and smaller than $\langle m_{\mathrm{exc}}^{z} \rangle$ in the 30-nm case within L_C of the contacts. We further notice that there is a small contribution to $\langle m_{\mathrm{exc}}^{z} \rangle$ beyond L_C on either side of the system. Therefore, despite the fact that the system iterates to self-consistency over the mean-field equations, the quantum

interference works to prematurely energetically separate the nested Fermi surfaces for the systems with layer widths of 20 nm and below. As the interlayer bias is increased, the quantum interference is exacerbated by the increased confinement in the 20-nm layers, and $\langle m_{exc}^z \rangle$ works to continue the energetic separation of the Fermi surfaces, which works to effectively close the gap and cut off the supercurrent flow in the layers. At this point, we return to the situation shown in Figs. 8 and 9, where we find no evidence of a gap or condensate.

IV. CONCLUSION

We have performed self-consistent quantum-transport calculations on bilayer graphene systems which are composed of two monolayers of graphene separated by a thin 1-nm SiO$_2$ tunnel dielectric in the regime of superfluidity. We find that, for layer widths greater that 20 nm in size, the system critical current can exceed the analytical values predicted by as much as 50%. This is due to the thermal smoothing of interlayer interactions allowing the Fermi surfaces to remain nested in energy longer than expected. We examined the system behavior before and after reaching the critical current through the analysis of the directional pseudospin fields. However, as we scale the widths of the layers down, we find an appreciable drop in the maximum critical current the system can sustain to roughly around 10% of the predicted analytical value. This results from reflections off of the energy gap which opens in the bulk of the system as a result of the formation of an exciton condensate. The quantum interference, which is exacerbated by the stronger confinement, works to energetically separate the nested Fermi surfaces and reduce the critical current in the bilayer graphene systems.

REFERENCES

[1] B. S. Doyle, S. Datta, M. Doczy, S. Hareland, B. Jin, J. Kavalieros, T. Linton, A. Murthy, R. Rios, and R. Chau, "High performance fully-depleted tri-gate CMOS transistors," *IEEE Electron Device Lett.*, vol. 24, no. 4, pp. 263–265, Apr. 2003.

[2] Y. Cui, Z. Zhong, D. Wang, W. U. Wang, and C. M. Lieber, "High performance silicon nanowire field effect transistors," *Nano Lett.*, vol. 3, no. 2, pp. 149–152, Jan. 2003.

[3] D. K. Ferry, M. J. Gilbert, and R. Akis, "Some considerations on nanowires and nanoelectronics," *IEEE Trans. Electron Devices*, vol. 55, no. 11, pp. 2820–2826, Nov. 2008.

[4] S. E. Thompson, M. Armstrong, C. Auth, S. Cea, R. Chau, G. Glass, T. Hoffman, J. Klaus, Z. Ma, B. Mcintyre, A. Murthy, B. Obradovic, L. Shifren, S. Sivakumar, S. Tyagi, T. Ghani, K. Mistry, M. Bohr, and Y. El-Mansy, "A logic nanotechnology featuring strained-silicon," *IEEE Electron Device Lett.*, vol. 25, no. 4, pp. 191–193, Apr. 2004.

[5] S. Datta, G. Dewey, M. Doczy, B. S. Doyle, B. Jin, J. Kavalieros, R. Kotlyar, M. Metz, N. Zelick, and R. Chau, "High mobility Si/SiGe strained channel MOS transistors with HfO$_2$/TiN gates," in *IEDM Tech. Dig.*, 2003, pp. 653–656.

[6] Y. Royter, K. R. Elliott, P. W. Deelman, D. H. Chow, I. Milsavljevic, and C. H. Fields, "High frequency InAs-channel HEMTs for low power ICs," in *IEDM Tech. Dig.*, 2003, pp. 731–734.

[7] T. Ashley, A. B. Dean, C. T. Elliott, R. Jefferies, F. Khaleque, and T. J. Phillips, "High-speed, low-power InSb transistors," in *IEDM Tech. Dig.*, 1997, pp. 751–754.

[8] K. Kalna, M. Borici, L. Yang, and A. Asenov, "Monte Carlo simulations of III–V MOSFETs," *Semicond. Sci. Technol.*, vol. 19, no. 4, pp. S202–S105, Mar. 2004.

[9] M. J. Gilbert and D. K. Ferry, "Indium arsenide quantum wire trigate metal–oxide–semiconductor field effect transistor," *J. Appl. Phys.*, vol. 99, no. 5, p. 054 503, Mar. 2006.

[10] P. J. Kuekes, D. R. Stewart, and R. S. Williams, "The crossbar latch: Logic value storage, restoration, and inversion in crossbar circuits," *J. Appl. Phys.*, vol. 97, no. 3, p. 034 301, Feb. 2005.

[11] K. Tsukagoshi, B. W. Alphenaar, and K. Nakazato, "Operation of logic function in a Coulomb blockade device," *Appl. Phys. Lett.*, vol. 73, no. 17, pp. 2515–2517, Oct. 1998.

[12] J. Appenzeller, Y.-M. Lin, J. Knoch, Z. Chen, and P. Avouris, "Comparing carbon nanotube transistors—The ideal choice: A novel tunneling device design," *IEEE Trans. Electron Devices*, vol. 52, no. 12, pp. 2568–2576, Dec. 2005.

[13] A. Liao, Y. Zhao, and E. Pop, "Avalanche-induced current enhancement in semiconducting carbon nanotubes," *Phys. Rev. Lett.*, vol. 101, no. 25, p. 256 804, Dec. 2008.

[14] I. B. Spielman, J. P. Eisenstein, L. N. Pfeiffer, and K. W. West, "Resonantly enhanced tunneling in a double layer quantum hall ferromagnet," *Phys. Rev. Lett.*, vol. 84, no. 25, pp. 5808–5811, Jun. 2000.

[15] M. J. Gilbert and J. Shumway, "Probing quantum coherent states in bilayer graphene," *J. Comput. Electron.*, vol. 8, no. 2, pp. 51–59, 2009.

[16] H. Min, R. Bistritzer, J.-J. Su, and A. H. MacDonald, "Room-temperature superfluidity in graphene bilayers," *Phys. Rev. B, Condens. Matter*, vol. 78, no. 12, p. 121 401, Sep. 2008.

[17] C.-H. Zhang and Y. N. Joglekar, "Exciton condensation of massless fermions in graphene bilayers," *Phys. Rev. B, Condens. Matter*, vol. 77, no. 23, p. 233 405, Jun. 2008.

[18] S. K. Banerjee, L. F. Register, E. Tutuc, D. Reddy, and A. H. MacDonald, "Bilayer pseudoSpin field-effect transistor (BiSFET): A proposed new logic device," *IEEE Electron Device Lett.*, vol. 30, no. 2, pp. 158–160, Feb. 2009.

[19] D. Reddy, L. F. Register, E. Tutuc, and S. K. Banerjee, "Bilayer pseudospin field-effect transistor: Applications to Boolean logic," *IEEE Trans. Electron Devices*, vol. 57, no. 4, pp. 755–764, Aug. 2010.

[20] A. K. Geim and K. S. Novoselov, "The rise of graphene," *Nat. Mater.*, vol. 6, no. 3, pp. 183–191, Mar. 2007.

[21] J.-J. Su and A. H. MacDonald, "How to make a bilayer exciton condensate flow," *Nat. Phys.*, vol. 4, pp. 799–802, 2008.

[22] T. Ando, "Exotic electronic and transport properties of graphene," *Phys. E*, vol. 40, no. 2, pp. 24–32, Dec. 2003.

[23] A. Rycerz, J. Tworzydlo, and C. W. J. Beenakker, "Valley filter and valley valve in graphene," *Nat. Phys.*, vol. 3, no. 3, pp. 172–175, Mar. 2007.

[24] A. H. MacDonald, "Superfluid properties of double-layer quantum Hall ferromagnets," *Phys. B*, vol. 298, no. 1, pp. 129–134, Apr. 2001.

[25] E. Rossi, A. S. Nunez, and A. H. MacDonald, "Interlayer transport in bilayer quantum hall systems," *Phys. Rev. Lett.*, vol. 95, no. 26, p. 266 804, Dec. 2005.

[26] M. J. Gilbert, "Finite temperature pseudospin torque effect in graphene bilayers," *Phys. Rev. B, Condens. Matter*, to be published.

[27] D. D. Johnson, "Modified Broyden method for accelerating convergence in self-consistent calculations," *Phys. Rev. B, Condens. Matter*, vol. 38, no. 18, pp. 12807–12813, Dec. 1988.

[28] A. J. Leggett, *Quantum Liquids: Bose Condensation and Cooper Pairing in Condensed-Matter Systems*. Oxford, U.K.: Oxford Univ. Press, 2006.

M. J. Gilbert (M'06) photograph and biography not available at the time of publication.